

Vibrational relaxation dynamics in layered perovskite quantum wells

Li Na Quan,^{1,2,*} Yoonjae Park,^{1,*} Peijun Guo,³ Mengyu Gao,^{2,4} Jianbo Jin,¹ Jianmei Huang,¹ Jason K. Copper,⁵ Adam Schwartzberg,⁶ Richard Schaller,³ David T. Limmer,^{1,2,5,7,†} and Peidong Yang^{1,2,5,7,4,‡}

¹*Department of Chemistry, University of California, Berkeley*

²*Materials Science Division, Lawrence Berkeley National Laboratory*

³*Center for Nanoscale Materials, Argonne National Laboratory*

⁴*Department of Materials Science and Engineering, University of California, Berkeley*

⁵*Chemical Science Division, Lawrence Berkeley National Laboratory*

⁶*Molecular Foundry, Lawrence Berkeley National Laboratory*

⁷*Kavli Energy NanoScience Institute, Berkeley, California, Berkeley*

(Dated: February 17, 2021)

Organic-inorganic layered perovskites are two-dimensional quantum wells with layers of lead-halide octahedra stacked between organic ligand barriers. The combination of their dielectric confinement and ionic sublattice results in excitonic excitations with substantial binding energies that are strongly coupled to the surrounding soft, polar lattice. However, the ligand environment in layered perovskites can significantly alter their optical properties due to the complex dynamic disorder of soft perovskite lattice. Here, we observe the dynamic disorder through phonon dephasing lifetimes initiated by ultrafast photoexcitation employing high-resolution resonant impulsive stimulated Raman spectroscopy of a variety of ligand substitutions. We demonstrate that vibrational relaxation in layered perovskite formed from flexible alkyl-amines as organic barriers is fast and relatively independent of the lattice temperature. Relaxation in aromatic amine based layered perovskite is slower, though still fast relative to pure inorganic lead bromide lattices, with a rate that is temperature dependent. Using molecular dynamics simulations, we explain the fast rates of relaxation by quantifying the large anharmonic coupling of the optical modes with the ligand layers and rationalize the temperature independence due to their amorphous packing. This work provides a molecular and time-domain depiction of the relaxation of nascent optical excitations and opens opportunities to understand how they couple to the complex layered perovskite lattice, elucidating design principles for optoelectronic devices.

Organic-inorganic hybrid layered perovskite quantum wells have optoelectronic properties that can be adapted to enable a diverse set of applications including solar cells, light-emitting diodes, semiconductor lasers, and photodetectors[1–6]. The structural stability and degree of quantum confinement can be tuned by varying the inorganic semiconductor, organic barrier compositions and stoichiometry independently, making them more viable for many device applications than their bulk counterparts[7–11]. The photoluminescence quantum efficiency of layered perovskites in particular can be altered by varying the molecular configuration of the organic ligands, and as a result, various compositions have been used for both light absorbing and light emitting applications[12–14]. The local distortions of the inorganic octahedra in layered perovskites create a complex energetic landscape for charges that activate additional

scattering mechanisms, and determine emergent optoelectronic properties such as exciton and carrier transport, and light emission[15]. However, the precise nature of electron lattice interactions in these materials remains to be understood. Femtosecond lasers have made it possible to impulsively generate and detect coherent phonons in semiconductor nanostructures with time-resolved pump and probe measurements. Time resolved photocarrier dynamics in quantum wells and semiconductor superlattices can provide detailed insight into the relevant interaction mechanisms between coherent phonons and coherently prepared electronic wave packets.

Here we employ ultrafast pump-probe transient absorption spectroscopy on 2D layered perovskites to investigate the direct dynamic interplay of optically generated excitons in the perovskite layer with their surrounding organic lattice. Our observations show a phonon dephasing process with a strong dependence on the organic barrier. In conjunction with molecular dynamics simulations, we find that the composition of organic ligands and inorganic quantum well thickness can substantially change the dephasing rate of optical phonons and their temper-

* These two authors contributed equally

† dlimmer@berkeley.edu

‡ p.yang@berkeley.edu

ature dependence, due to varying degrees of anharmonicity in the lattice and dynamic structural disorder. This molecular and time domain insight into optical relaxation sheds light on the emergent electron-lattice interactions in these materials and enables their design for optoelectronic devices.

We studied thin films and single crystals of A_2PbX_4 ($A=R-NH_3^+$) that can be synthesized by mixing precursors at desired stoichiometric ratios, followed by spontaneous self-assembly of the quantum well structure, illustrated in Fig. 1A (see details in Methods). This class of materials is known to exhibit moderate quantum confinement effects, resulting in narrow-band emission (bandwidth eV) combined with exceptionally large oscillator strength ($7 \times 10^{-2}cm^{-1}$)[16]. Optical phonons are expected to be the most strongly coupled modes to nascent electronic excitations in these materials as such optical phonons will modulate charge transport and Coulomb screening[17–19]. Such motions can in principle be investigated by Raman scattering by examining the lineshapes which informs the lifetime, enabling the elucidation of the roles of confinement, extended interfaces, and disorder on the modes[20]. However, these are often difficult to disentangle in highly complex systems which have inherently coupled broadening mechanisms.

By employing a narrow optical excitation and following the excitation in the time domain from the associated transient modulation of the reflectivity, we can decouple the effects from homogeneous and inhomogeneous broadening in the Raman scattering lineshape. Femtosecond optical excitation allows for an impulsive coherent electronic excitation that generates coherent phonons as it relaxes, as it is shorter than the inverse of the phonon period[21]. Since the generation and subsequent relaxation processes are strongly affected by the coupling of phonon modes to the photoexcited states, the real-time observation of coherent phonons can offer crucial insight into the dynamic electron-phonon coupling.

To detect the coherent phonons, we use a standard pump-probe configuration in which the observed differential transmission (dT) is modulated due to changes in the complex dielectric function from electron-phonon coupling. Thus, the dephasing time can be characterized by the decay of the dT modulation amplitude. Using time-resolved measurements, it has been possible to monitor the dephasing of coherent optical phonons near $q = 0$ in polar semiconductors such as GaP[22], GaAs[23], ZnSe[22], InP[24]. In Figs. 1B and C, we show that the dT dynamics in the thin films following resonant excitation with a sub-50-fs visible pulse (3.26 eV). The vibrational coherence map can be resolved due to the spec-

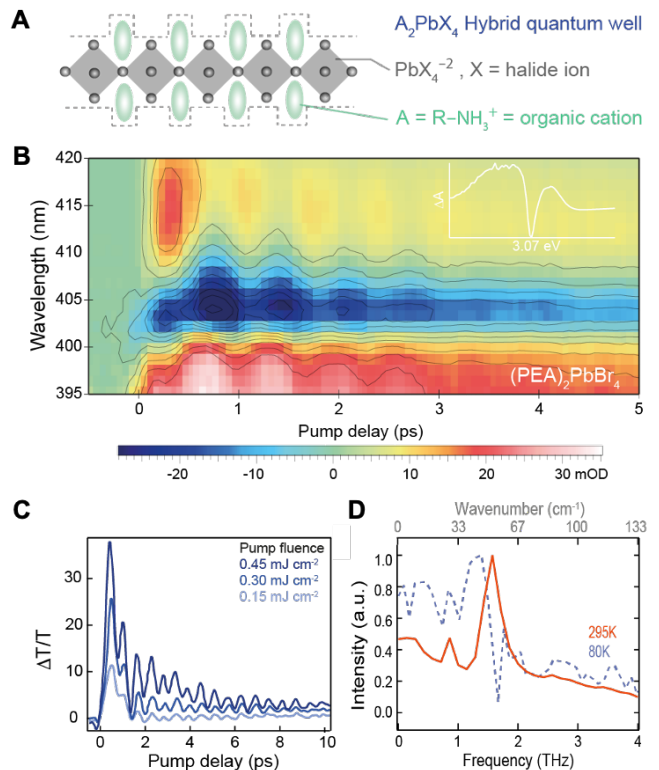


FIG. 1. Impulsive generation of coherent phonon oscillations in $(PEA)_2PbBr_4$. (A) Schematic illustration of the hybrid quantum-well structure. (B) Time-resolved differential transmission (dT) spectrum from $(PEA)_2PbBr_4$. (C) Extracted coherent phonon oscillations from time-resolved differential transmission spectrum measured with different pump intensity at 80K. Probe energy of 3.0 eV. (D) Fourier transform spectrum of the coherent oscillation measured at room temperature (red solid lines) and 80 K (blue dashed lines).

trally dispersed probe-wavelength and collected as a function of pump-probe delay time and probe wavelength. We observed pronounced oscillations resulting from optical phonons on top of an exponentially decaying background. The background signal is related to rapid electronic excited state relaxation. In bulk perovskites such as $CsPbX_3$, a coherent phonon induced oscillation is less visible due to the decrease in both phonon mode amplitude and dephasing rate at room temperature[25]. The dT oscillations can be assigned to two different phonon modes with frequency calculated by fast Fourier transform of 0.85 THz (wavenumber) and 1.57 THz (wavenumber), as shown in Fig. 1D. We also measured the photoexcited phonon dynamics at various pump wavelengths with both off-resonance and resonant excitations (3.5- 2.9 eV). We observed oscillatory response in all cases (Fig. S6), indicative of a strong coupling of optical excitation to the lattice.

We considered one ligand derived from an alkyl group, n-butylamine (BTA), and one from an aromatic group, phenylethylamine (PEA). The packing geometry of the organic barriers leads to a structural deformation of inorganic octahedral (Fig. S2), and thus strongly affects the energy, lifetime, and localization of the band-edge exciton, and as a result, affects changes to the electrical transport properties of these materials[26, 27]. We observed a clear trend in photoluminescence efficiency, where the perovskites with aromatic organic groups typically shown high photoluminescent yield of up to 50 % at room temperature while those made of alkyl groups show much lower yields. Therefore, a comprehensive understanding of their dynamical structure under photoexcitation is important for the development of an efficient materials platform. The stable phase of $(\text{PEA})_2\text{PbBr}_4$ is a lattice with a triclinic space group (P1), and the PEA organic barriers stack in a T-shape arrangement via strong $\pi - \pi$ interaction, forming relatively rigid crystal geometry. The $(\text{BTA})_2\text{PbBr}_4$ perovskites, on the other hand, form a lattice with a Pbcn space group, with the alkyl-group organic cations generating a weak quantum well-to-well stacking interaction indicated by the relatively broad diffraction peaks (Fig. S2). Fig. 2A reports the ultrafast resonant impulsive Raman probed at 3.0 eV for both $(\text{PEA})_2\text{PbBr}_4$ and $(\text{BTA})_2\text{PbBr}_4$, where the oscillation spectra have been obtained after subtraction of an exponential decay of carriers. This oscillation observed is reproducible for different positions on the sample. Upon photoexcitation, we observe qualitatively different dynamics depending on the organic barriers. For $(\text{PEA})_2\text{PbBr}_4$, we find persistent oscillations over 5 ps, while for $(\text{BTA})_2\text{PbBr}_4$, oscillations are dephased rapidly and any mode assignment becomes uncertain. The corresponding ultrafast phonon-dephasing rate extracted was significantly diminished in the perovskites with the alkyl group, relative to the aromatic group. These measurements were repeated at different temperatures, spanning 80 K to 300 K. Additionally, we also varied alkyl chain lengths, and the shape of aromatic groups and measured their corresponding phonon dephasing dynamics (Fig. S7).

The spectral fringe visibility of the resulting optical phonon vibrations, as a function of time delay, is used to measure the phonon dephasing time. This is extracted and plotted as a function of temperature in Fig. 2B. In $(\text{PEA})_2\text{PbBr}_4$, it showed a strong temperature-dependent phonon dephasing rate, indicative of the anharmonicity of optical phonon coupled to the electronic states. The coherent phonon population in $(\text{PEA})_2\text{PbBr}_4$ perovskites decays within 4-5 ps at room temperature,

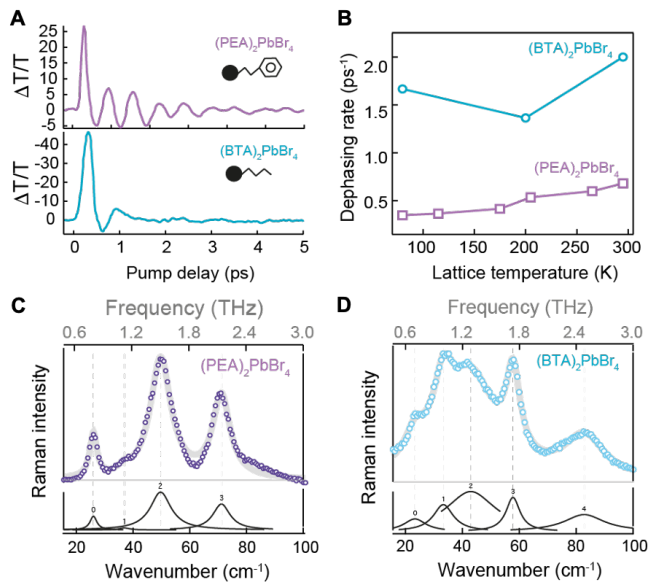


FIG. 2. Structural information of hybrid perovskite quantum wells with different organic ammonium cation as barriers and the corresponding phonon-lattice dynamics. (A) Resonant impulsive Raman spectra by pump-probe measurement with quantum wells packed with different geometry at room temperature. TA is plotted at the probe energy of 3.0 eV. (B) Lattice temperature dependent dephasing rate of coherent optical phonon dynamics. Non-Resonant Raman spectra (fitted with Lorentzian) of (C) $(\text{PEA})_2\text{PbBr}_4$ perovskite quantum well and (D) $(\text{BTA})_2\text{PbBr}_4$ perovskite quantum well.

while the dephasing time can be extended up to 10 ps at 80 K. This increase of the phonon relaxation rate with temperature is anticipated by the increase phonon-scattering enabled by anharmonic effects in the vibrational potential energy[28, 29]. In $(\text{BTA})_2\text{PbBr}_4$, with alkyl chain group, the dephasing rate was around 4 times faster than the aromatic ligand. Further the dephasing rate in the alkyl ligand had no significant temperature dependence. In bulk crystalline semiconductors, a temperature independent phonon linewidth is usually explained as consequence of an elastic scattering of coherent phonons by a perturbing potential of lattice defects[30]. However, as we discuss below, in this case it is a high degree of dynamic rather than static disorder that results in a suppressed temperature dependence in $(\text{BTA})_2\text{PbBr}_4$. Given a common inorganic framework, the different temperature dependence observed for the different cations indicates that the organic ligands play an important role in determining the lifetime of the modes most strongly coupled to the photogenerated excitons.

To gain initial insight into the optical phonons and their structural disorder, we further performed non-

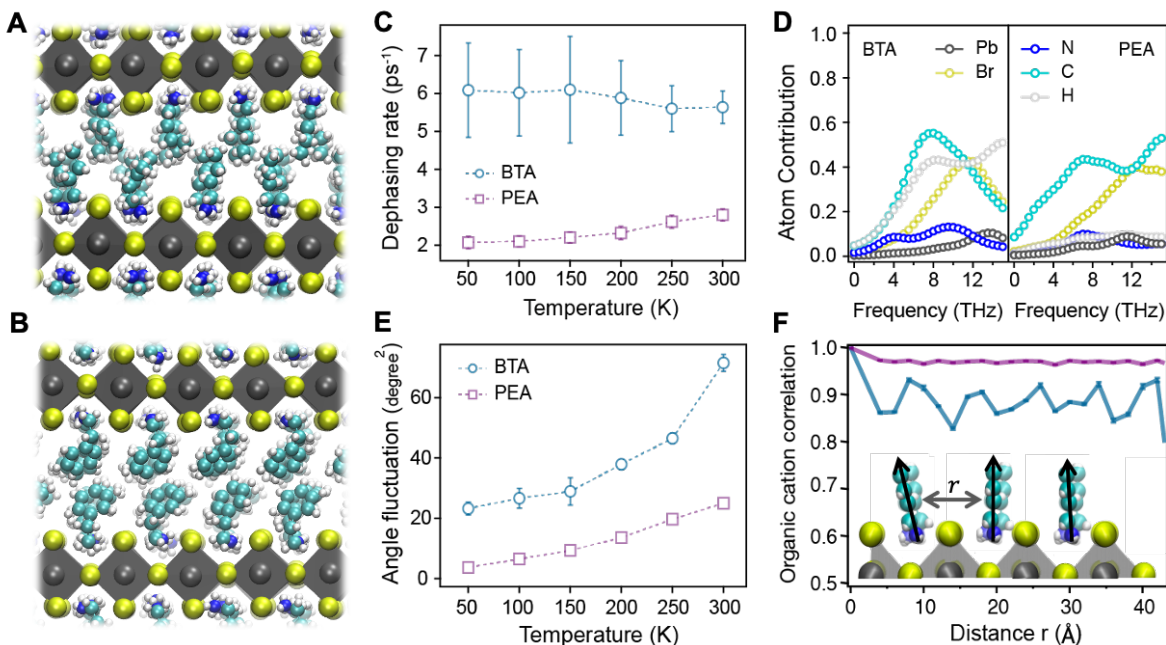


FIG. 3. Simulation of vibrational dynamics. (A,B) Snapshots of simulations on (BTA)₂PbBr₄ (A) and (PEA)₂PbBr₄ (B) perovskites. Colored dots below are the color schemes for the snapshots. (C) Dephasing rate of the lowest optical mode in (BTA)₂PbBr₄ (blue circles) and (PEA)₂PbBr₄ (purple squares). (D) Contributions from each atom type to the vibrational mode as a function of frequencies of vibrational mode in each layered perovskite. (E) Fluctuations of angles between vertical axis and NC vector (schematically defined in Fig. S14) at each temperature. (F) Normalized spatial correlations between the nitrogen-carbon dipole vector (black arrows) as a function of the lateral distance between vectors. Dotted lines in (C) and (E) are guides to the eye.

resonant Raman scattering measurements with all perovskites we mentioned previously. The low-frequency (10–100 cm⁻¹) Raman scattering is expected to be associated with vibrational information of inorganic octahedral, and thus uniquely suited to measure the distortion induced modulated structures. We observed in Fig. 2C, three strong symmetric vibrational scattering feature below 100 cm⁻¹ in (PEA)₂PbBr₄, which previously assigned to various vibrational modes of PbBr₆ octahedral frameworks. Especially the strongest vibrational scattering at 55 cm⁻¹ is well matched with optical phonon oscillation frequency that we observed from time-resolved optical measurements. Surprisingly, we found a significant broadening and spectral shift of inorganic phonon modes in perovskites with alkyl group (BTA)₂PbBr₄, shown in Fig. 2D, which is characteristically associated with inhomogeneous distortion in the octahedral lattice. The Raman signal at 40 cm⁻¹ is a sum of two broadened symmetric Lorentzian subpeaks of Pb-Br coordination, which means the Pb-Br bond lengths in (BTA)₂PbBr₄ are distorted significantly compare with the (PEA)₂PbBr₄. The Raman result implying that the variable orientation of the different organic cations is largely responsible for the

lattice distortion.

To obtain an atomistic perspective on the vibrational dynamics of (BTA)₂PbBr₄ and (PEA)₂PbBr₄, we performed molecular dynamics simulations. To simulate each perovskite, we employed an empirical model (Tables S1-3) with fixed point charges whose reduced computational cost enables the study of extended system sizes over the long times required to average over the slow fluctuations of the ligands[31, 32]. While simple, the model reasonably reproduces experimental values of the lattice constants and mechanical properties of these and related materials (Table S4). Snapshots of the simulations with the different organic cations are shown in Fig. 3A and 3B. To study the dynamics of vibrational relaxation, we extract the phonon modes by computing the lattice Green’s function and solving the associated eigenvalue equation from the dynamical matrix. We employ the fluctuation dissipation theorem to compute the dynamical matrix from the displacement correlations from a simulation at 50 K, and extract the effective vibrational frequencies and phonon modes (Eq. S6) at that temperature[33, 34]. It is expected that optical phonons with lower energy are attributed to the bending and rocking motions of PbX₃

inorganic framework[20, 35, 36]. While we confirm that they participate in these modes, in our calculations we found that the organic cations contribute significantly to the low-frequency modes in the layered perovskites. The participation ratio for each atom type as a function of frequency is shown in Fig. 3D, where for both PEA and BTA cations the organic ligand atoms contribute up to 40% to the longitudinal and transverse optical modes.

For the lowest frequency optical mode in each layered perovskite, we computed the dephasing rate over a range of temperatures from 50 K to 300 K. In the classical limit, the Fermi's golden rule rate for vibrational relaxation, Γ_λ , can be computed by the Fourier transform of the force-force correlation function of the optical mode[37],

$$\Gamma_\lambda = \frac{1}{k_B T} \int_0^\infty dt \cos(\omega_\lambda t) \langle F_\lambda(0) F_\lambda(t) \rangle$$

where F_λ is the force on the λ 'th mode due to the anharmonic coupling to the surrounding lattice and ω_λ its corresponding frequency. The average $\langle \dots \rangle$ is taken over an isobaric, isothermal ensemble with 1 atm of pressure and varying temperature. The classical treatment of the nuclei is justified by the fact that the energy for the optical phonon is much less than the thermal energy, $\hbar\omega_\lambda \ll k_B T$, where \hbar , k_B , and T are Planck's constant, Boltzmann's constant and the temperature respectively [38]. In agreement with experiment, Fig. 3C shows the dephasing rates in $(\text{BTA})_2\text{PbBr}_4$ are higher than the rates for $(\text{PEA})_2\text{PbBr}_4$ across the range of temperatures studied. Further consistent with the experiment, we find a strong temperature dependence of the dephasing rate with the PEA cation, while the dephasing rate with the BTA cation is insensitive to the temperature.

We find that the high phonon dephasing rates in both $(\text{PEA})_2\text{PbBr}_4$ and $(\text{BTA})_2\text{PbBr}_4$ are a consequence of significant anharmonic coupling of the optical mode to the ligand barriers that increase phonon scattering. We have characterized the anharmonicity both directly through structural measures and indirectly through the dependence of the modes on temperature and volume. To quantify anharmonicity structurally within the perovskites, we analyzed the angle distribution of each organic cation. Fig. 3E shows the mean squared fluctuations of the angle, $\langle \delta\Theta^2 \rangle$, between the axis perpendicular to the inorganic octahedra plane, $\hat{\mathbf{z}}$, and the nitrogen-carbon unit vector, \mathbf{R}_{NC} , as a function of each temperature, such that $\cos(\Theta) = \mathbf{R}_{\text{NC}} \cdot \hat{\mathbf{z}}$. If the local potential of the ligand orientation were harmonic, according to the fluctuation-dissipation theorem the fluctuations would increase linearly as the temperature is increased. For both the PEA and BTA cations, we find a nonlinear tem-

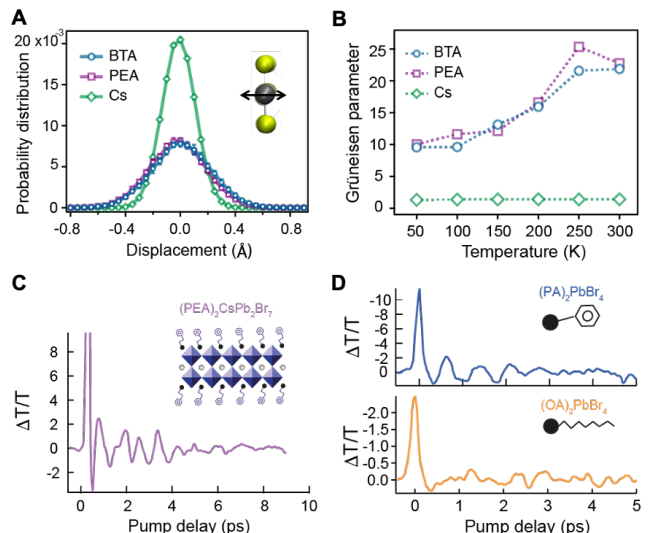


FIG. 4. Generality and mitigation of coherent phonon dephasing dynamics. (A) Probability distribution of Pb atom displacement from its average position in $(\text{BTA})_2\text{PbBr}_4$ (blue circles), $(\text{PEA})_2\text{PbBr}_4$ (purple squares), and CsPbBr_3 (green diamonds) perovskites. (B) Grüneisen anharmonicity parameters in layered and bulk perovskites. Dotted lines are used to connect neighboring symbols. Oscillatory response from coherent phonon dynamics of (C) $n = 2$ multi-quantum well perovskites with PEA organic cations and (D) $n = 1$ quantum well perovskites with phenylammonium (top) and octylammonium (bottom) organic cations.

perature dependence, with a more significant departure from linearity in BTA relative to PEA. The corresponding distribution, (Fig. S14), is significantly non-Gaussian for BTA, while only marginally so for PEA at 300 K. Both have optical frequencies that show a strong temperature dependence (Fig. S11), while for BTA the optical mode becomes significantly mixed with increasing temperature (Fig. S10). Given the large contribution of the ligand to the optical mode in both materials, the stronger anharmonicity of $(\text{BTA})_2\text{PbBr}_4$ than in $(\text{PEA})_2\text{PbBr}_4$ explains the higher rate of phonon relaxation in BTA perovskite as resulting from stronger phonon scattering.

The relative temperature independence of $(\text{BTA})_2\text{PbBr}_4$ can be understood by noting the significant dynamic disorder in that lattice relative to $(\text{PEA})_2\text{PbBr}_4$. This is quantified by the spatial correlation between nitrogen-carbon dipoles, $\boldsymbol{\mu}$,

$$C(r) = \langle \boldsymbol{\mu}(0) \cdot \boldsymbol{\mu}(r) \rangle$$

separated by a lateral distance r . This correlation function is illustrated in Fig. 3F, normalized by its value at the origin, $C(r)/C(0)$. For $(\text{PEA})_2\text{PbBr}_4$, the normalized correlation function, which ranges from 0 to 1,

is unstructured, and does not decay appreciably over 40 Å. For $(\text{BTA})_2\text{PbBr}_4$, however, the correlation decreases within a unit cell, and drops periodically to as low as 0.8. Compared to PEA, the lower long-ranged correlation in BTA details an amorphous packing of BTA even at low temperature. Rather than the expected phonon-defect scattering, this shows that the persistent dynamic disorder results in a temperature insensitive relaxation rate. Molecularly this results from the stronger, directional $\pi - \pi$ stacking of PEA as shown in Fig. 3B, relative to the weaker isotropic van der Waals interactions of BTA.

We have compared these simulation findings to a CsPbBr_3 bulk perovskite, by considering two additional measures of anharmonicity. At the molecular level, we analyze the structure of the inorganic framework. We have computed the displacement distribution of the lead atoms from their equilibrium lattice positions at 300 K. Fig. 4A illustrates that the distribution is much narrower in CsPbBr_3 perovskite relative to $(\text{PEA})_2\text{PbBr}_4$ or $(\text{BTA})_2\text{PbBr}_4$, indicating that structures of layered perovskites are soft and less structurally rigid as compared to bulk perovskite, while the distributions are nearly identical for both ligands. Additionally, we have calculated the Grüneisen parameter, $\gamma_\lambda = -\partial \ln \omega_\lambda / \partial \ln V$, for the λ 'th mode with lattice volume V (Fig. S13). Since the frequency of harmonic modes does not depend on the volume and temperature, a higher value of Grüneisen parameter indicates a higher strength of anharmonicity. Fig. 4B shows γ for the lowest optical model as a function of temperature. We find that the anharmonicity in layered perovskites is much higher than in the bulk perovskite, consistent with our expectation, and the former grows with temperature. Using an Umklapp scattering model [39], the Grüneisen parameter and the corresponding lower shear moduli of the layered perovskites are qualitatively able to reproduce the ordering of the dephasing rates of $(\text{BTA})_2\text{PbBr}_4$ and $(\text{PEA})_2\text{PbBr}_4$, and suggest that both are an order of magnitude larger than that expected for CsPbBr_3 (Fig. S12).

While the direct comparison to the bulk CsPbBr_3 perovskite is not possible experimentally due to the decreased phonon amplitude and facile charge separation, we have studied the vibrational dynamics of lattices with increased inorganic layers. We synthesized a single crystal $(\text{PEA})_2\text{CsPb}_2\text{Br}_7$ ($n = 2$) perovskite and measured its ultrafast coherent optical phonon dynamics. The transient absorption signal is shown in Fig. 4C in which the dephasing lifetime is longer, 8 ps, compared with single layered $(\text{PEA})_2\text{PbBr}_4$ ($n = 1$) counterpart. This is consistent with mitigating the anharmonic coupling

to the ligand barriers, and subsequent lower phonon-to-phonon scattering rates. Additionally, as a direct test of the underlying molecular packing argument emerging from the simulations, we synthesized and measured the coherent phonon dynamics of $(\text{PA})_2\text{PbBr}_4$ where PA is Phenylammonium and $(\text{OA})_2\text{PbBr}_4$ where OA is Octylammonium perovskites. Fig. 4D demonstrates that the phonon lifetime is longer with the PA organic cation, as clarified by its persistent oscillatory response, as compared to the OA organic cation, in which no oscillations are observed. This is consistent with the ability of aromatic cations to leverage $\pi - \pi$ interactions and stabilize a more ordered ligand layer relative to alkyl cations, supporting the previous analysis of the BTA and PEA organic cations.

We have presented an experimental and theoretical description of vibrational relaxation in layered perovskites. We studied the dephasing dynamics of two different organic cations in depth and observed a difference in lifetime and response to the temperature of the phonons, implying that organic cations play an important role in determining the relaxation dynamics coupled to photogenerated excitations. This work elucidates that anharmonicity and dynamic disorder from organic cations facilitates vibrational relaxation and optical vibrational modes are largely mixed with the organic species. Our work contributes to the deeper understanding of phonon dynamics and may provide the foundation for future studies on the mechanism of electron-phonon interaction in Ruddlesden-Popper phase perovskites.

ACKNOWLEDGMENTS

This work was supported by the U.S. Department of Energy, Office of Science, Office of Basic Energy Sciences, Materials Sciences and Engineering Division, under Contract No. DE-AC02-05-CH11231 within the Physical Chemistry of Inorganic Nanostructures Program (KC3103). This research used resources of the National Energy Research Scientific Computing Center, a U.S. Department of Energy Office of Science User Facility operated under Contract No. DE-AC02-05CH11231. Simon Teat and Laura McCormick are acknowledged for helping to accommodate the single-crystal X-ray beamtime. Use of the Center for Nanoscale Materials, an Office of Science user facility, was supported by the U.S. Department of Energy, Office of Science, Office of Basic Energy Sciences, under Contract No. DE-AC02-06CH11357. The Raman system acquisition was supported by the NSF MRI proposal (EAR-1531583).

-
- [1] D. B. Mitzi, C. Feild, W. Harrison, and A. Guloy, *Nature* **369**, 467 (1994).
- [2] B. Saparov and D. B. Mitzi, *Chem. Rev.* **116**, 4558 (2016).
- [3] Z.-K. Tan, R. S. Moghaddam, M. L. Lai, P. Docampo, R. Higler, F. Deschler, M. Price, A. Sadhanala, L. M. Pazos, D. Credgington, F. Hanusch, T. Bein, H. J. Snaith, and R. H. Friend, *Nat. Nanotechnol.* **9**, 687 (2014).
- [4] M. M. Lee, J. Teuscher, T. Miyasaka, T. N. Murakami, and H. J. Snaith, *Science* **338**, 643 (2012).
- [5] H. Zhu, Y. Fu, F. Meng, X. Wu, Z. Gong, Q. Ding, M. V. Gustafsson, M. T. Trinh, S. Jin, and X.-Y. Zhu, *Nat. Mater.* **14**, 636 (2015).
- [6] Y. Fu, H. Zhu, J. Chen, M. P. Hautzinger, X.-Y. Zhu, and S. Jin, *Nat. Rev. Mater.* **4**, 169 (2019).
- [7] K. Chondroudis and D. B. Mitzi, *Chem. Mater.* **11**, 3028 (1999).
- [8] Y. Chen, Y. Sun, J. Peng, J. Tang, K. Zheng, and Z. Liang, *Adv. Mater.* **30**, 1703487 (2018).
- [9] M. Yuan, L. N. Quan, R. Comin, G. Walters, R. Sabatini, O. Voznyy, S. Hoogland, Y. Zhao, E. M. Beauregard, P. Kanjanaboos, *et al.*, *Nat. Nanotechnol.* **11**, 872 (2016).
- [10] C. C. Stoumpos, D. H. Cao, D. J. Clark, J. Young, J. M. Rondinelli, J. I. Jang, J. T. Hupp, and M. G. Kanatzidis, *Chem. Mater.* **28**, 2852 (2016).
- [11] B. Dhanabalan, Y.-C. Leng, G. Biffi, M.-L. Lin, P.-H. Tan, I. Infante, L. Manna, M. P. Arciniegas, and R. Krahne, *ACS Nano* **14**, 4689 (2020).
- [12] X. Gong, O. Voznyy, A. Jain, W. Liu, R. Sabatini, Z. Piontkowski, G. Walters, G. Bappi, S. Nokhrin, O. Bushuyev, *et al.*, *Nat. Mater.* **17**, 550 (2018).
- [13] L. Dou, A. B. Wong, Y. Yu, M. Lai, N. Kornienko, S. W. Eaton, A. Fu, C. G. Bischak, J. Ma, T. Ding, *et al.*, *Science* **349**, 1518 (2015).
- [14] Y. Gao, E. Shi, S. Deng, S. B. Shiring, J. M. Snaider, C. Liang, B. Yuan, R. Song, S. M. Janke, A. Liebman-Peláez, *et al.*, *Nat. Chem.* **11**, 1151 (2019).
- [15] M. Z. Mayers, L. Z. Tan, D. A. Egger, A. M. Rappe, and D. R. Reichman, *Nano Lett.* **18**, 8041 (2018), 1811.04726.
- [16] C. M. Mauck and W. A. Tisdale, *Trends Chem.* **1**, 380 (2019).
- [17] F. Thouin, D. A. Valverde-Chávez, C. Quarti, D. Cortecchia, I. Bargigia, D. Beljonne, A. Petrozza, C. Silva, and A. R. S. Kandada, *Nat. Mater.* **18**, 349 (2019).
- [18] M. Sendner, P. K. Nayak, D. A. Egger, S. Beck, C. Müller, B. Epping, W. Kowalsky, L. Kronik, H. J. Snaith, A. Pucci, and R. Lovrinčić, *Mater. Horiz.* **3**, 613 (2016), 1607.08541.
- [19] H. Wang, L. Valkunas, T. Cao, L. Whittaker-Brooks, and G. R. Fleming, *J. Phys. Chem. Lett.* **7**, 3284 (2016).
- [20] A. C. Ferreira, S. Paofai, A. Létoublon, J. Ollivier, S. Raymond, B. Hehlen, B. Rufflé, S. Cordier, C. Katan, J. Even, and P. Bourges, *Commun. Phys.* **3**, 48 (2020), 2001.05445.
- [21] M. Hase, M. Kitajima, A. M. Constantinescu, and H. Petek, *Nature* **426**, 51 (2003).
- [22] W. E. Bron, J. Kuhl, and B. K. Rhee, *Phys. Rev. B* **34**, 6961 (1986).
- [23] F. Vallée and F. Bogani, *Phys. Rev. B* **43**, 12049 (1991).
- [24] F. Vallée, *Phys. Rev. B* **49**, 2460 (1993).
- [25] P. Nėmec and P. Malý, *Phys. Rev. B* **72**, 235324 (2005).
- [26] D. B. Straus, N. Iotov, M. R. Gau, Q. Zhao, P. J. Carroll, and C. R. Kagan, *J. Phys. Chem. Lett.* **10**, 1198 (2019).
- [27] J. Hu, I. W. H. Oswald, S. J. Stuard, M. M. Nahid, N. Zhou, O. F. Williams, Z. Guo, L. Yan, H. Hu, Z. Chen, X. Xiao, Y. Lin, Z. Yang, J. Huang, A. M. Moran, H. Ade, J. R. Neilson, and W. You, *Nat. Commun.* **10**, 1276 (2019).
- [28] M. Balkanski, R. F. Wallis, and E. Haro, *Phys. Rev. B* **28**, 1928 (1983).
- [29] P. Verma, S. C. Abbi, and K. P. Jain, *Phys. Rev. B* **51**, 16660 (1995).
- [30] M. Hase, K. Ishioka, M. Kitajima, K. Ushida, and S. Hishita, *Appl. Phys. Lett.* **76**, 1258 (2000).
- [31] T. Hata, G. Giorgi, K. Yamashita, C. Caddeo, and A. Mattoni, *J. Phys. Chem. C* **121**, 3724 (2017).
- [32] A. Mattoni, A. Filippetti, and C. Caddeo, *J. Phys.: Condens. Matter* **29**, 043001 (2016).
- [33] L. T. Kong, *Comput. Phys. Commun.* **182**, 2201 (2011).
- [34] M. Dove, *École thématique de la Société Française de la Neutronique* **12**, 123 (2011).
- [35] N. S. Dahod, A. France-Lanord, W. Paritmongkol, J. C. Grossman, and W. A. Tisdale, *J. Chem. Phys.* **153**, 044710 (2020).
- [36] M. Nagai, T. Tomioka, M. Ashida, M. Hoyano, R. Akashi, Y. Yamada, T. Aharen, and Y. Kanemitsu, *Phys. Rev. Lett.* **121**, 145506 (2018).
- [37] S. Egorov, K. Everitt, and J. Skinner, *J. Phys. Chem. A* **103**, 9494 (1999).
- [38] J. Skinner and K. Park, *J. Phys. Chem. B* **105**, 6716 (2001).
- [39] J. M. Ziman, *Electrons and phonons: the theory of transport phenomena in solids* (Oxford university press, 2001).

Supplementary Materials for

Vibrational relaxation dynamics in layered perovskite quantum wells

Li Na Quan^{1,2,8}, Yoonjae Park^{1,8}, Peijun Guo⁷, Mengyu Gao^{2,5}, Jianbo Jin¹, Jianmei Huang¹,
Jason K. Copper³, Adam Schwartzberg⁶, Richard Schaller⁷, David T. Limmer^{1,2,3,4*}, and Peidong
Yang^{1,2,3, 4,5*}

¹ *Department of Chemistry, University of California, Berkeley*

² *Materials Science Division, Lawrence Berkeley National Laboratory*

³ *Chemical Science Division, Lawrence Berkeley National Laboratory*

⁴ *Kavli Energy NanoScience Institute, Berkeley, California, Berkeley*

⁵ *Department of Materials Science and Engineering, University of California, Berkeley*

⁶ *Molecular Foundry, Lawrence Berkeley National Laboratory*

⁷ *Center for Nanoscale Materials, Argonne National Laboratory*

⁸ *These authors contributed equally*

Simulation details

Numerical model and simulation protocols.

We consider two different types of layered perovskites, $(\text{BTA})_2\text{PbBr}_4$ and $(\text{PEA})_2\text{PbBr}_4$, and bulk perovskite, CsPbBr_3 . BTA stands for butylammonium, which has a long carbon chain, and PEA stands for phenylethylammonium, which has benzene ring. To simulate perovskites with molecular dynamics (MD), we first made an initial configuration of each perovskite. The distances between Pb and Br atoms are set to 3.616 initially. In organic cations (BTA or PEA), relative positions, charges of atoms, and indices for bonds, angles, dihedrals are from LigParGen server¹⁻³. The interaction potential between atoms is described in details in the force field section below. Calculations for layered and bulk perovskites are performed using $6 \times 4 \times 6$ and $8 \times 8 \times 8$ unit cells respectively.

For equilibration of layered and bulk perovskites, MD simulations are run in a constant temperature and pressure ensemble (NPT) for 500ps with the timestep 0.5fs for layered and 1.0fs for bulk perovskites at 300K and 1atm. The time parameters for Nosé-Hoover thermostat/barostat⁴ are 250fs, 150fs, and 400fs for $(\text{BTA})_2\text{PbBr}_4$, $(\text{PEA})_2\text{PbBr}_4$, and CsPbBr_3 perovskites respectively. For $\text{PEA}_2\text{PbBr}_4$ perovskite, we run additional NPT equilibration run with the time parameter of 500fs. After equilibration, configurations are stored in every 100ps and each of them becomes a restart point for the production run. In order to calculate dephasing rate, we run 350ps simulation to get converged dynamical matrix for both layered and bulk perovskites. Additionally, to get force-force autocorrelation function, we run 6ps and 12ps NPT simulations for layered and bulk perovskites respectively. The time parameter of 10ps is used for thermostat/barostat in all perovskites where we checked that force-force autocorrelation functions are insensitive to the value and results are not statistically distinguishable. Details on how to get and use vibrational modes to calculate the dephasing rate are described in the section below. Dephasing rates are computed by running 30, 20, and 10 trajectories for $(\text{BTA})_2\text{PbBr}_4$, $(\text{PEA})_2\text{PbBr}_4$, and CsPbBr_3 perovskites respectively. For the calculation at the temperature other than 300K, we add 500ps NPT simulation to gradually drop the temperature from 300K to each temperature and run 200ps for the equilibration purposes at the dropped temperature before calculating properties. The

equations of motion are integrated with a Verlet algorithm, with long ranged forces employing an Ewald summation, both as implemented in LAMMPS ⁵.

Force fields for layered and bulk perovskites.

In organic-inorganic perovskites, the total potential energy is the sum of inorganic–inorganic, U_{II} , organic–organic, U_{OO} , and inorganic–organic, U_{IO} , interactions. We adopt the classical force field from Mattoni *et al* ⁶ for $U_{\text{II}} = U_{\text{Buck}} + U_{\text{Coul}}$, known as Buckingham-Coulomb (BC) potential, which includes the short-ranged repulsive interactions, attractive terms due to the dispersive forces, and long-range electrostatic interactions.

$$U_{\text{Buck}} = \sum_{i,j} A_{ij} e^{-r_{ij}/\rho_{ij}} - \frac{c_{ij}}{r_{ij}} \quad , \quad U_{\text{Coul}} = \sum_{i,j} \frac{q_i q_j}{4\pi\epsilon_0 r_{ij}} \quad (\text{S.1})$$

r_{ij} is the distance between atoms i and j , A , ρ , and c are parameters for Buckingham potential, ϵ_0 is the vacuum electric permittivity, and q_i is an atomic charge of atom i . The interaction potential for U_{IO} is described by the sum of BC potential and Lennard-Jones potential with electrostatic terms. Lennard-Jones (LJ) potential is written as:

$$U_{\text{LJ}} = \sum_{i,j} 4\epsilon_{ij} \left[\left(\frac{\sigma_{ij}}{r_{ij}} \right)^{12} - \left(\frac{\sigma_{ij}}{r_{ij}} \right)^6 \right] \quad (\text{S.2})$$

where ϵ and σ are parameters for LJ potential. Parameters for interatomic interactions with Buckingham potential are listed in Table S1.

U_{OO} is based on a generalized AMBER force field (GAFF) ^{7,8} which has bonded and nonbonded interactions. Bonded interactions are described by the sum of three potentials to prevent bond breaking and maintain the structure of organic cations during the simulation as follows:

$$\begin{aligned} U_{\text{OO,bonded}} &= U_{\text{bonds}} + U_{\text{angles}} + U_{\text{dihedrals}} \\ &= K_b(r - r_0)^2 + K_a(\theta - \theta_0)^2 + K_d[1 + \cos(n\phi - d)] \end{aligned} \quad (\text{S.3})$$

where the coefficients of each potential are borrowed from GAFF. Nonbonded interactions include U_{Coul} electrostatic and U_{LJ} dispersive contributions. All non-bonded interatomic interactions which are not listed in Table S1 can be derived from Lorentz-Berthelot rules using parameters listed in Table S3. For the force fields for bulk perovskite CsPbBr₃, we use slightly different Buckingham

parameters⁹ which are listed in Table S2. To validate our models, in Table S4, we listed the lattice constants and mechanical properties at room temperature for layered and bulk perovskites from both simulations and experiments where results from simulations make a reasonable agreement with the values from experiment and other related materials. For mechanical properties, we also compared Young's modulus of $\text{BTa}_2\text{PbBr}_4$ perovskite (2.96 ± 1.15 GPA) with experimental result of lead-halide layered perovskite¹⁰ and checked that bulk modulus of CsPbBr_3 (23.46 ± 4.67 GPA) is consistent with values from other theoretical calculations¹¹⁻¹³.

Vibrational modes from MD simulation.

To get the frequency and direction of vibrational modes, we adopt the method of diagonalizing the dynamical matrix from MD simulations employing the fluctuation-dissipation theorem. Assuming that the atoms are vibrating around their equilibrium positions, the total potential energy U can be expressed in terms of lattice vibration u as follow:

$$U = U_0 + \sum_i \left(\frac{\partial U}{\partial u_i} \right) u_i + \frac{1}{2} \sum_i u_i \Phi_{ij} u_j + \frac{1}{3!} \sum_{i,j,k} \left(\frac{\partial^3 U}{\partial u_i \partial u_j \partial u_k} \right)_0 u_i u_j u_k + \dots \quad (\text{S.4})$$

where $\Phi_{ij} = \left(\partial^2 U / \partial u_i \partial u_j \right)_0$, U_0 is the minimum value of potential energy, subscript 0 indicates that the derivatives are calculated at the equilibrium positions, and index i and j go over all atoms and dimensions. In the harmonic approximation where terms higher than second order are assumed to be negligible, the total potential energy at equilibrium is written as the third term in the Eq. S.4. From the fluctuation-dissipation theorem, force constant between atoms i and j , Φ_{ij} , is related to the inverse of the second moment of lattice vibrations $\langle u_i u_j \rangle$, defined as Green's function G_{ij} by a factor of $k_B T$, i.e. $G_{ij} = \langle u_i u_j \rangle$ and $\Phi_{ij} = k_B T (G^{-1})_{ij}$. Ensemble average is denoted as $\langle \dots \rangle$. In our simulations, the Green's functions are measured every 10fs and 20fs for layered and bulk perovskites respectively and acoustic sum rule is applied with 100 iterations¹⁴.

In periodic system, such as ionic crystals, it is convenient to describe vibrations in terms of wave vectors where modes with different wave vectors are not coupled to each other. Our calculations are performed at the gamma point and from force constant matrix, dynamical matrix can be obtained as:

$$\mathbf{D}_{ij}(\mathbf{q}) = \frac{1}{\sqrt{m_i m_j}} \Phi_{ij}(\mathbf{q}) \quad (\text{S.5})$$

where the frequencies of vibrational modes at each wave vector are computable through the solution of the eigenvalue equation

$$\omega^2(\mathbf{q}) \cdot \mathbf{e} = \mathbf{D}(\mathbf{q}) \cdot \mathbf{e} \quad (\text{S.6})$$

where ω is the vibrational frequency and \mathbf{e} is corresponding phonon mode. Details on the lattice dynamics and phonon measurements are described in ¹⁴⁻¹⁶.

In this framework, at each wave vector, each eigenvalue ω_λ^2 has a corresponding eigenvector $\vec{\mathbf{e}}_\lambda$ which has the information on the direction of the vibrational mode λ . Since eigenvectors are normalized,

$$\sum_{j=1}^n \sum_{\alpha=x,y,z} e_{\alpha j}^2 = 1 \quad (\text{S.7})$$

where n represents the number of atoms in the unit cell, values in $\vec{\mathbf{e}}_\lambda$ act as the probability amplitude in the mode λ . $e_{\alpha j}^2$ can be considered as the contribution of atom j to the vibrational mode λ with the frequency ω_λ in the direction α . In Figure 3D, Lorentzian distribution which is centered at ω_λ with the width η , $L(\omega, \omega_\lambda, \eta)$, is summed over all the vibrational modes.

$$L(\omega, \omega_\lambda, \eta) = \frac{1}{\pi\eta} \left[\frac{\eta^2}{(\omega - \omega_\lambda)^2 + \eta^2} \right] \quad (\text{S.8})$$

Since the area under the curve for atom j is proportional to the value of $\sum_{\alpha=x,y,z} e_{\alpha j}^2$, at each frequency, the value for atom j has the information on how much the contribution of atom j to the vibrational mode with that frequency is. In this calculation, $\eta = 1.511$ and $\eta = 1.478$ are used in $(\text{BTA})_2\text{PbBr}_4$ and $(\text{PEA})_2\text{PbBr}_4$ perovskites, respectively.

In Figure S10, a dot product between $\vec{\mathbf{e}}$ with the lowest nonzero frequency at 50K and $\vec{\mathbf{e}}$ at other temperatures is plotted, which indicates how similar the vibrational modes at higher temperatures are with the modes at 50K. The value ranges from 1 (parallel) to 0 (orthogonal). For $(\text{PEA})_2\text{PbBr}_4$ and CsPbBr_3 perovskites, the values from dot product are close to 1 for the whole range of temperatures, meaning that the modes are not changed upon the increase of the temperature. However, for $(\text{BTA})_2\text{PbBr}_4$ perovskite, the direction of the lowest vibrational mode is changed a lot as temperature is increased, indicating that it has much larger anharmonicity compared to other

perovskites. \vec{e} at each temperature are obtained by averaging 30/20/10 trajectories in (BTA)₂PbBr₄ / (PEA)₂PbBr₄ / CsPbBr₃ perovskites.

Dephasing rate calculation.

The excited vibrational states are relaxed by interacting with other degrees of freedoms. If the interaction is weak, the vibrational relaxation rate (dephasing rate) can be computed from Fermi's Golden Rule:

$$\Gamma_{i \rightarrow f} = \frac{1}{\hbar^2} \int_0^\infty dt e^{i\omega t} \langle \hat{V}(t) \hat{V}(0) \rangle \quad (\text{S.9})$$

where \hat{V} is the quantum mechanical operator of the coupling between states. If \hat{V} is expanded perturbatively in terms of vibrational modes of the system up to the first order, then, assuming that modes are harmonic and upward and downward transitions are balanced by each other, in the classical limit $\hbar\omega \ll k_B T$ where \hbar is Planck's constant divided by 2π and k_B is Boltzmann's constant, dephasing rate of the vibrational mode λ with the frequency ω is written as follows^{17,18}:

$$\Gamma_\lambda = \beta \int_0^\infty dt \cos(\omega_\lambda t) \langle F_\lambda(t) F_\lambda(0) \rangle \quad (\text{S.10})$$

where $\beta = 1/k_B T$ and F_λ is the force acting on the mode λ from the environment. Quantum mechanical force correlation function in the integral in Eq. S.10 is replaced by the classical counterpart multiplied by the quantum correction factor, ζ . In the first order perturbative approach, exact expression for ζ is known as

$$\zeta = \frac{\hbar\omega}{2k_B T} \frac{1}{\tanh(\beta\hbar\omega/2)} \quad (\text{S.11})$$

which is approximately 1 in the frequency and temperature range we are interested in.

In our calculations using Eq. S.10, for each mode λ , ω_λ and \vec{e}_λ from the diagonalization of dynamical matrix are used and forces acting on vibrational mode λ , F_λ , is obtained from the forces in the real space as follow:

$$F_\lambda(t) = \sum_{j=1}^n \sum_{\alpha=x,y,z} \frac{1}{\sqrt{m_j}} e_{\alpha j}(\lambda) F_{\alpha j}(t) \quad (\text{S.12})$$

where n is the number of atoms in a unit cell. Details on the Eq. S.12 which connects the positions in real space and vibrational modes is discussed in ¹⁶.

Correction of dephasing rate

Anharmonic interactions result in the decay of phonons through phonon-phonon scattering, which for optical modes are expected to be dominated by Umklapp scattering. The dephasing rate of vibrational modes through Umklapp process is computable as:

$$\Gamma_U = 2\gamma^2 \frac{k_B T}{G V_0} \frac{\omega^2}{\omega_D} \quad (\text{S.13})$$

where Γ_U is the dephasing rate of a specific vibrational mode, γ is the Grüneisen parameter described in the section below, G is the shear modulus, V_0 is the volume per atom, ω_D is the Debye frequency, and ω is the frequency of vibrational mode.

According to the Eq. S.13, at a given temperature in each perovskite, dephasing rate has quadratic scaling with the vibrational frequency, indicating that the discrepancy between higher dephasing rate between the simulation and experiment can be attributed to the higher frequencies in the former. Since frequencies predicted from MD simulations are higher than the frequencies measured from Raman scattering due to fixed charges in MD simulations, we checked that the scale of dephasing rates predicted from theory makes an agreement with experiment quantitatively by multiplying the ratio of ω^2 from experiments to simulations. Within this analysis, in explaining the dephasing rate through Umklapp process, we assumed that the difference in value of dephasing rate is dominated by the frequency difference between simulation and experiment. Difference in other thermodynamic parameters T , V_0 (lattice constants), and μ are quite small.

In Figure S12, we use Eq. S.13 to compute dephasing rate. To estimate rates through Umklapp scattering, we use Grüneisen parameter γ described in Figure 4B and μ , V_0 , and ω at low temperature. Even though dephasing rates from Umklapp scattering are much higher than the rates predicted from Eq. S.10, they make a qualitative agreement in terms of ordering where rates of (BTA)₂PbBr₄ perovskite are higher than the rates of (PEA)₂PbBr₄ perovskite.

Grüneisen anharmonicity parameter

Anharmonic interactions cause the vibrational modes to be relaxed. One of the ways to quantify anharmonicity of the system is to calculate Grüneisen parameter γ defined as:

$$\gamma = -\frac{V}{\omega} \frac{\partial \omega}{\partial V} \quad (\text{S.14})$$

If all the vibrational modes are harmonic, then the frequency does not depend on the volume. In terms of our simulations, since simulations are performed at the constant pressure and temperature, the way to change the volume is to change the temperature of simulations. The derivative of frequency with respect to volume in Eq S.14 is approximated by the fitting described in Figure S13 and the volume V and the lowest frequency ω at each temperature are used to calculate γ .

Structural analysis

We found that the structure of organic cations has the information on the disorder and anharmonicity in perovskites. In Figure S14, black arrows indicate the axis perpendicular to the inorganic octahedra plane, $\hat{\mathbf{z}}$, and colored arrows represent the vector from the nitrogen N to the last carbon C in each organic cation, \mathbf{R}_{NC} . From the probability distribution of angles between $\hat{\mathbf{z}}$ and vector \mathbf{R}_{NC} , distribution from $(\text{BTA})_2\text{PbBr}_4$ perovskite is much broader than the one from $(\text{PEA})_2\text{PbBr}_4$, indicating that organic cations in BTA perovskites are less ordered compared to organic cations in PEA perovskites. As the way of quantifying anharmonicity, at each temperature, we measured the width of the distribution (angle fluctuation) by calculating the standard deviation. If the interaction potential is purely harmonic, from fluctuation-dissipation theorem, the fluctuation is linearly scaled by the temperature. In Figure 3E, the angle fluctuation in $(\text{BTA})_2\text{PbBr}_4$ perovskites has nonlinear increase as temperature is increased, which is the signature of anharmonicity in the system.

i	j	A_{ij} (kcal/mol)	ρ_{ij} (Å)	c_{ij} (kcal/mol/ Å ⁶)
Pb	Pb	74933300.560633	0.1232469484	0.0000
Pb	Br	110223.381656	0.3021004695	0.0000
Pb	N	32690390.937994	0.1509470000	0.0000
Pb	C/C _a	32690390.937994	0.1509470000	0.0000
Br	Br	24274.905590	0.4528610329	654.4127155
Br	N	94836.351976	0.3352375000	0.0000
Br	C/C _a	94836.351976	0.3352375000	0.0000

TABLE S1. Parameters for Buckingham potential (Eq. S.1). The carbon atoms in the benzene rings are indicated by C_a.

i	j	A_{ij} (kcal/mol)	ρ_{ij} (Å)	c_{ij} (kcal/mol/ Å ⁶)
Pb	Pb	70359906.629702	0.131258	0.0000
Pb	Br	110555.046796038	0.30119416859	0.0000
Pb	Cs	5199160.12131845	0.201404	0.0000
Br	Br	24347.9494383149	0.451502449901	0.0000
Br	Cs	96716.7648844106	0.3615262249505	0.0000
Cs	Cs	384185.64295958	0.27155	0.0000

TABLE S2. Parameters for Buckingham potential (Eq. S.1) in CsPbBr₃ perovskite.

i	ϵ_i (kcal/mol)	σ_i (Å)
Pb	0.012484076	3.45998
Br	0.16729697	3.8416142857
N	0.1700	3.24999852378
C	0.1094	3.39966950842
C_a	0.0860	3.39966950842
H_n	0.0157	1.06907846177
H_x	0.0157	1.95997717991
H_c	0.0157	2.64953278775
H_a	0.0150	2.59964245953

TABLE S3. Parameters for Lennard-Jones potential (Eq. S.2). Parameters for all pairwise interaction potential can be completed by the following combining rules, $\epsilon_{ij} = \sqrt{\epsilon_i \epsilon_j}$ and $\sigma_{ij} = (\sigma_i + \sigma_j)/2$. The hydrogen atoms in ammonium NH_3^+ group and the benzene ring are indicated by H_n and H_a , respectively. H_x indicates the hydrogen atoms which are next to positively charged group and other hydrogen atoms in the carbon chains are represented as H_c .

	$(\text{BTA})_2\text{PbBr}_4$		$(\text{PEA})_2\text{PbBr}_4$		CsPbBr_3	
	sim.	ref.	sim.	ref.	sim.	ref.
a (Å)	5.97	5.84	12.47	11.62	8.6	8.7 ¹⁹
b (Å)	5.97	5.84	12.34	11.62	8.6	8.7 ¹⁹
c (Å)	30.27	27.55	17.08	17.62	8.6	8.7 ¹⁹
α (°)	—	—	89.98	99.49	—	—
β (°)	—	—	100.98	105.71	—	—
γ (°)	—	—	90.00	90.03	—	—
B (GPa)	4.16	—	0.44	—	21.35	21.56 ¹²
E (GPa)	3.77	3.3 ¹⁰	3.87	—	25.55	—

TABLE S4. Lattice constants and mechanical properties (B , bulk modulus and E , Young's modulus) of both layered and bulk perovskites from simulation and other related materials for comparison.

Experimental methods

Fabrication of perovskite thin films.

To prepare the layered perovskite thin film, PbBr_2 (0.5 M) (99.999% Sigma-Aldrich) and $\text{R-NH}_3\text{Br}$ (R =organic group) (1M) (Phenylethylammonium bromide (PEABr) or Phenylammonium bromide (PABr) or Butylammonium bromide (BTABr) or n-propyl ammonium bromide (nPABr) or Octylammonium bromide (OABr)) (Greatcell Solar Materials) were dissolved in DMSO. The mixed precursor solution was spin-coated on the glass substrate and follow by annealing at 90°C for 10 min.

Synthesis of perovskite single crystals.

To prepare the $(\text{R-NH}_3)_2\text{PbBr}_4$ perovskite single crystals, PbBr_2 and $\text{R-NH}_3\text{Br}$ were dissolved in a mixed DMSO and DMF (7:3) solution and 0.5 ml of solution was placed in a vial, the vial placed inside a larger container with chloroform solvent. The combined container was leave under the room temperature for 12 to 24 hrs. After the crystallization process, the crystals were rinsed with chloroform and dried inside the vacuum oven.

To prepare the $(\text{PEA})_2\text{CsPb}_2\text{Br}_7$ ($n=2$) perovskite single crystals, crystallization with slow cooling saturated HBr solution was used instead. Appropriate ratio of PEABr, PbBr_2 and CsBr were mixed in 9M HBr . The mixture was heated up to 120°C to get fully dissolved after stirring for 4 hours, and slowly cooling down to room temperature at a rate of $\sim 2^\circ\text{C/hr}$. Phase pure PEA version $n=2$ is hard to achieved due to phase separation, therefore, additional CsBr (PEABr : PbBr_2 : CsBr = 2.5 : 5 : 4) will be added for $(\text{PEA})_2\text{CsPb}_2\text{Br}_7$ single crystals synthesis. After the crystallization process, the crystals were rinsed with chloroform and dried inside the vacuum oven. $(\text{PEA})_2\text{CsPb}_2\text{Br}_7$ ($n=2$) single crystals was picked up and verified with Photoluminescence (PL) before further measurements.

Single Crystal X-ray Diffraction Structure Determination

Single crystal X-ray diffraction (SCXRD) data was collected with synchrotron X-ray radiation at the Advanced Light Source (ALS) at the Lawrence Berkeley National Lab (LBNL) at beamline 12.2.1. The data was collected at 100K, on a BrukerD8 diffractometer equipped with PHOTON 100 CCD detector and using silicon (111) monochromated synchrotron radiation ($\lambda = 0.7288 \text{ \AA}$).

A plate-shaped single crystal of $(\text{PEA})_2\text{CsPb}_2\text{Br}_7$ ($n=2$) was mounted on a MiTegen Kapton loop and placed in the cyro N_2 steam of an Oxford Cryosystem Plus for Data Collection. The raw data were processed with the Bruker APEX3 software. The data were first integrated using the SAINT and then corrected for absorption with SADABS (APEX3, version 8.38; Bruker-AXS: Madison, WI 2018.; SADABS, Version 2014/4; Bruker-AXS: Madison, WI 2014). The structures were solved by Intrinsic with SHELXT-2018 and refined on full-matrix least squares on F^2 with SHELXL-2018²⁰⁻²² using the Olex2 software package²³. The Crystal structures are visualized by VESTA software²⁴.

Ultrafast differential transmission measurements.

Ultrafast differential transmission measurements were performed using a 35-fs Ti:sapphire amplifier with output at 800 nm at a repetition rate of 2 kHz. The broadband probe pulses were generated by focusing a portion of the amplifier output onto a 2-mm thick CaF_2 window. The pump pulses were produced by an optical parametric amplifier and reduced in repetition rate down to 1 kHz using an optical chopper. The sample is loaded into a liquid-nitrogen cryostat with vacuum level better than 1×10^{-6} Torr.

Chemical Formula	(C ₈ H ₉ NH ₃) ₂ CsPb ₂ Br ₇
Formula weight	1351.03
Temperature/K	273.15
Crystal system	monoclinic
Space group	C2/c
a/Å	11.4983(4)
b/Å	11.5424(4)
c/Å	44.8235(19)
α /°	90
β /°	97.315(2)
γ /°	90
Volume/Å ³	5900.5(4)
Z	8
$\rho_{\text{calc}}/\text{cm}^3$	3.042
μ/mm^{-1}	22.102
F(000)	4784.0
Crystal size/mm ³	0.062 × 0.041 × 0.005
Radiation	$\lambda = 0.72880$
2 Θ range for data collection/°	3.664 to 48.816
Index ranges	-13 ≤ h ≤ 13, -13 ≤ k ≤ 13, -52 ≤ l ≤ 52
Reflections collected	89079
Independent reflections	4840 [R _{int} = 0.0766, R _{sigma} = 0.0308]
Data/restraints/parameters	4840/0/189
Goodness-of-fit on F ²	1.073
Final R indexes [I ≥ 2 σ (I)]	R ₁ = 0.0456, wR ₂ = 0.1008
Final R indexes [all data]	R ₁ = 0.0537, wR ₂ = 0.1047
Largest diff. peak/hole / e Å ⁻³	2.05/-2.21

TABLE S5. Crystal data and structure refinement details of the SCXRD data for (PEA)₂CsPb₂Br₇ (n=2).

Atom	x	y	z	U11	U22	U33	U23	U13	U12
Pb1	7194.7(4)	7120.5(4)	6821.1(2)	11.9(2)	10.0(2)	31.1(3)	-0.44(19)	0.8(2)	-0.61(18)
Pb2	12130.8(4)	7123.2(4)	6820.5(2)	13.5(2)	10.1(2)	31.1(3)	-0.20(19)	7.7(2)	0.25(18)
Cs1	10000	9747(2)	7500	21.4(7)	120.3(16)	20.6(7)	0	2.8(5)	0
Cs2	10000	4567.5(13)	7500	127.3(17)	22.8(7)	21.9(7)	0	2.4(8)	0
Br6	6725.0(11)	7018.0(11)	6153.9(3)	19.9(6)	18.0(6)	18.2(7)	1.1(5)	2.2(5)	-0.3(5)
Br7	11931.4(11)	7008.6(11)	6153.0(3)	20.1(6)	19.1(6)	17.9(7)	0.6(5)	2.2(5)	0.2(5)
Br4	12787.0(11)	4639.3(11)	6841.2(3)	19.7(6)	9.6(6)	29.8(7)	0.4(5)	2.3(5)	0.2(5)
Br3	6556.6(11)	4638.7(10)	6840.8(3)	20.9(6)	8.8(6)	29.8(7)	0.9(5)	5.5(5)	-0.1(5)
Br1	4669.9(11)	7681.8(11)	6833.8(3)	13.6(6)	21.1(7)	29.5(7)	-3.5(6)	4.4(5)	-0.5(5)
Br2	9670.7(11)	6408.6(11)	6834.3(3)	12.5(6)	21.8(7)	34.2(8)	0.4(6)	4.4(5)	-0.2(5)
Br5	7508.4(15)	7134.5(14)	7500.2(3)	44.0(8)	39.1(8)	15.5(6)	-0.5(6)	2.2(6)	-0.7(7)
C11	4323(16)	4185(14)	6153(3)	58(3)	29(2)	27(2)	-2.1(18)	4(2)	0(2)
C12A	4610(30)	4210(30)	5823(7)	58(3)	29(2)	27(2)	-2.1(18)	4(2)	0(2)
C12B	3720(30)	4270(30)	5825(7)	58(3)	29(2)	27(2)	-2.1(18)	4(2)	0(2)
C13A	3680(30)	4850(30)	5625(7)	58(3)	29(2)	27(2)	-2.1(18)	4(2)	0(2)
C13B	4480(40)	4850(30)	5622(7)	58(3)	29(2)	27(2)	-2.1(18)	4(2)	0(2)
C14	4032(16)	6009(14)	5540(3)	58(3)	29(2)	27(2)	-2.1(18)	4(2)	0(2)
C15A	2930(30)	6610(30)	5353(7)	58(3)	29(2)	27(2)	-2.1(18)	4(2)	0(2)
C15B	4990(30)	6590(30)	5360(7)	58(3)	29(2)	27(2)	-2.1(18)	4(2)	0(2)
C16A	1930(30)	6030(30)	5254(7)	58(3)	29(2)	27(2)	-2.1(18)	4(2)	0(2)
C16B	5870(30)	6030(30)	5266(7)	58(3)	29(2)	27(2)	-2.1(18)	4(2)	0(2)
C17	6373(16)	4861(14)	5318(3)	58(3)	29(2)	27(2)	-2.1(18)	4(2)	0(2)
C18A	2640(30)	4310(30)	5510(7)	58(3)	29(2)	27(2)	-2.1(18)	4(2)	0(2)
C18B	5400(30)	4280(30)	5515(7)	58(3)	29(2)	27(2)	-2.1(18)	4(2)	0(2)
C21	9309(16)	4655(15)	6144(3)	58(3)	29(2)	27(2)	-2.1(18)	4(2)	0(2)
C22A	9430(30)	4220(30)	5825(7)	58(3)	29(2)	27(2)	-2.1(18)	4(2)	0(2)
C22B	8820(40)	4150(30)	5824(7)	58(3)	29(2)	27(2)	-2.1(18)	4(2)	0(2)
C23A	8560(30)	4830(30)	5617(7)	58(3)	29(2)	27(2)	-2.1(18)	4(2)	0(2)
C23B	9560(30)	4850(30)	5608(7)	58(3)	29(2)	27(2)	-2.1(18)	4(2)	0(2)
C24	8991(16)	5973(14)	5540(3)	58(3)	29(2)	27(2)	-2.1(18)	4(2)	0(2)
C25A	7870(30)	6570(30)	5351(7)	58(3)	29(2)	27(2)	-2.1(18)	4(2)	0(2)
C25B	9910(30)	6570(30)	5349(7)	58(3)	29(2)	27(2)	-2.1(18)	4(2)	0(2)
C26A	6860(30)	6000(30)	5246(7)	58(3)	29(2)	27(2)	-2.1(18)	4(2)	0(2)
C26B	10850(30)	6040(30)	5239(7)	58(3)	29(2)	27(2)	-2.1(18)	4(2)	0(2)
C27	1420(16)	4907(14)	5316(3)	58(3)	29(2)	27(2)	-2.1(18)	4(2)	0(2)
C28A	7530(30)	4300(30)	5501(7)	58(3)	29(2)	27(2)	-2.1(18)	4(2)	0(2)
C28B	10480(30)	4300(30)	5505(7)	58(3)	29(2)	27(2)	-2.1(18)	4(2)	0(2)
N1	4396(13)	5366(11)	6281(3)	58(3)	29(2)	27(2)	-2.1(18)	4(2)	0(2)
N2A	8490(30)	4590(20)	6274(6)	58(3)	29(2)	27(2)	-2.1(18)	4(2)	0(2)
N2B	10280(20)	4570(20)	6273(6)	58(3)	29(2)	27(2)	-2.1(18)	4(2)	0(2)

TABLE S6. Fractional Atomic Coordinates ($\times 10^4$) and Anisotropic displacement factor ($\text{\AA}^2 \times 10^3$) of $(\text{PEA})_2\text{CsPb}_2\text{Br}_7$.

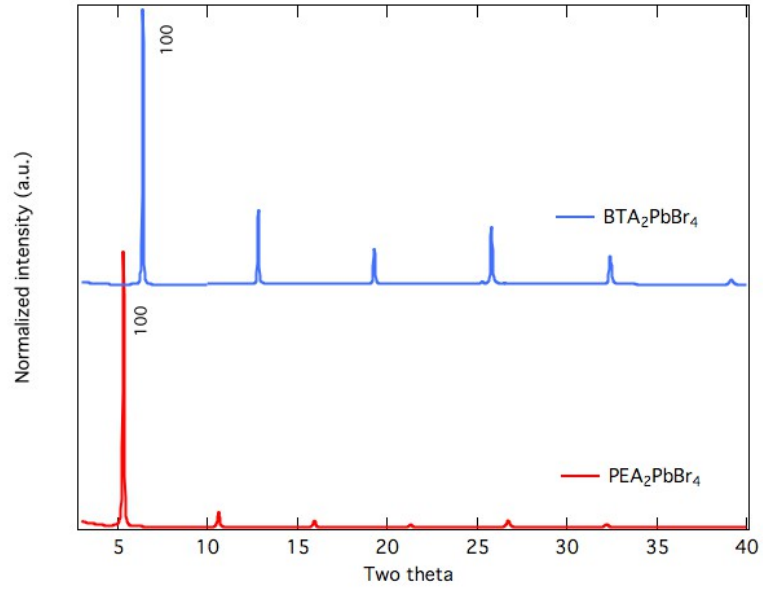


FIG. S1. X-ray diffraction of $(\text{BTA})_2\text{PbBr}_4$ and $(\text{PEA})_2\text{PbBr}_4$ perovskite thin films on the glass substrate.

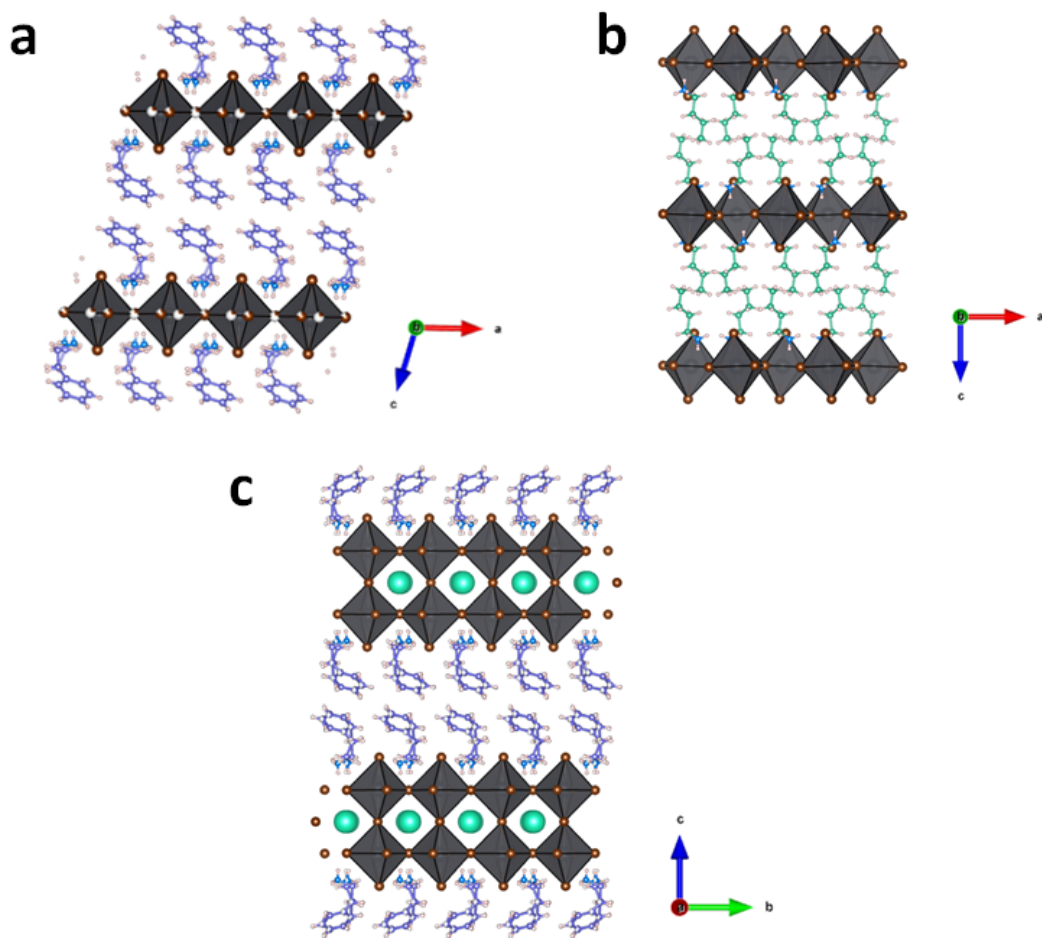


FIG. S2. Crystal structure of a) $(\text{PEA})_2\text{PbBr}_4$, b) $(\text{BTA})_2\text{PbBr}_4$ and c) $(\text{PEA})_2\text{CsPb}_2\text{Br}_7$ single crystals from single crystal X-ray diffraction measurements.

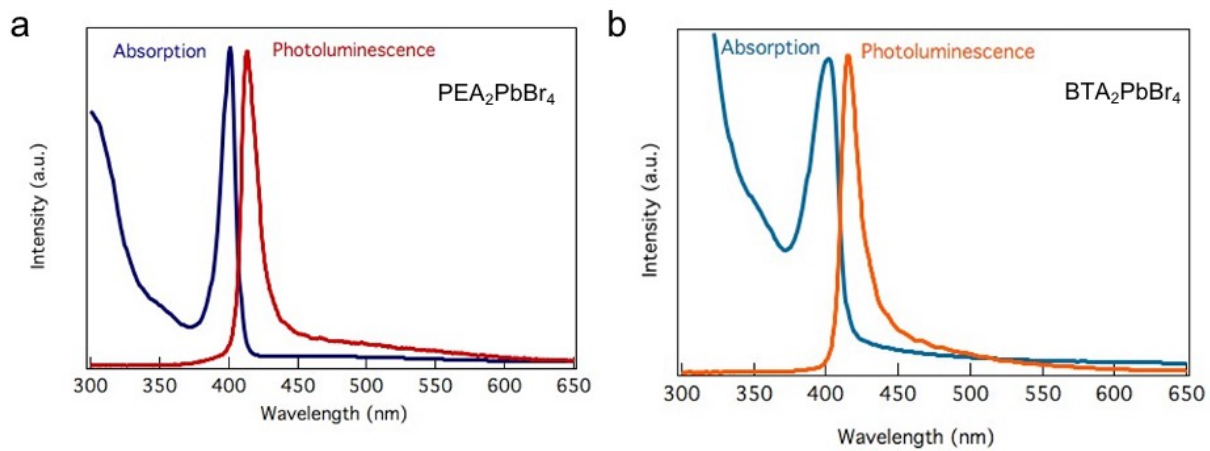


FIG. S3. Absorption and photoluminescence of $(\text{PEA})_2\text{PbBr}_4$ and $(\text{BTA})_2\text{PbBr}_4$ layered perovskites.

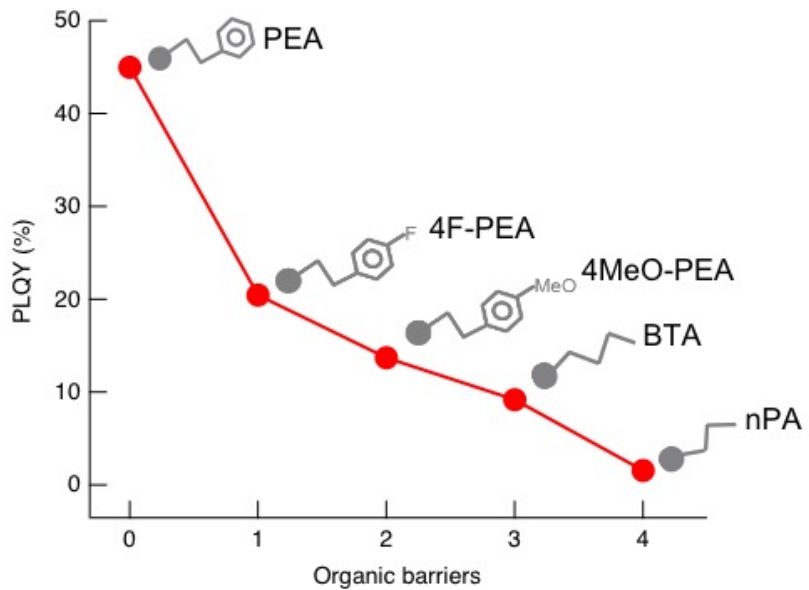


FIG. S4. Photoluminescence quantum efficiency of $(R-NH_3)_2PbBr_4$ layered perovskites as function of various organic cations.

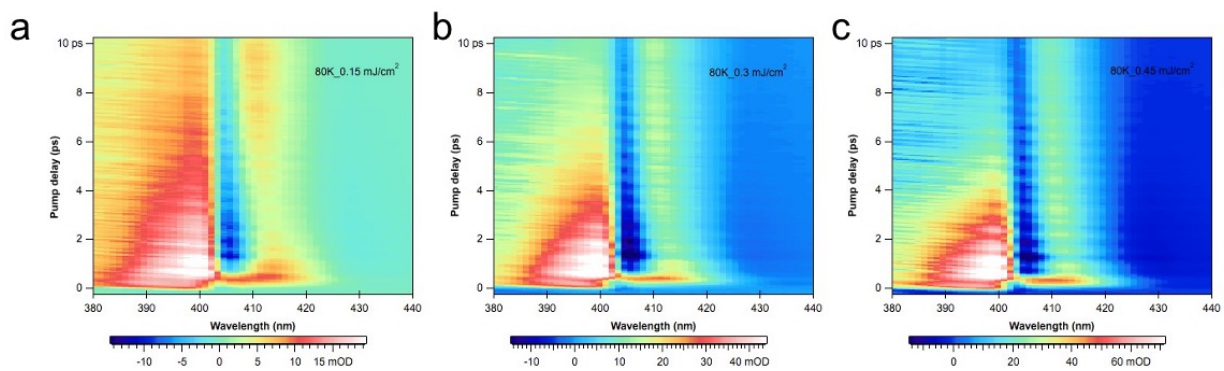


FIG. S5. Transient absorption spectra maps of $(\text{PEA})_2\text{PbBr}_4$ at 80K temperature with various pump fluences and 3.12 eV in pump wavelength.

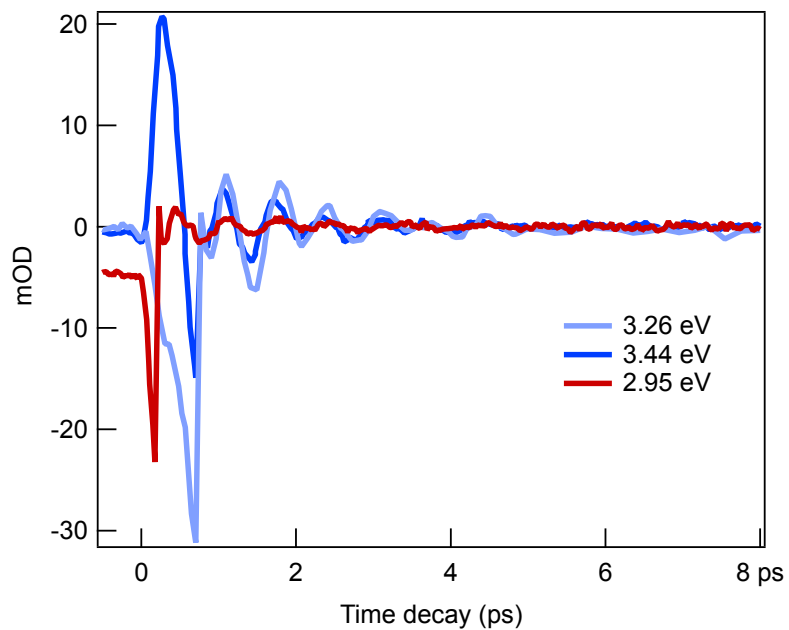


FIG. S6. Coherent phonon oscillation curves (band edge) of $(\text{PEA})_2\text{PbBr}_4$ perovskite at different pump energy.

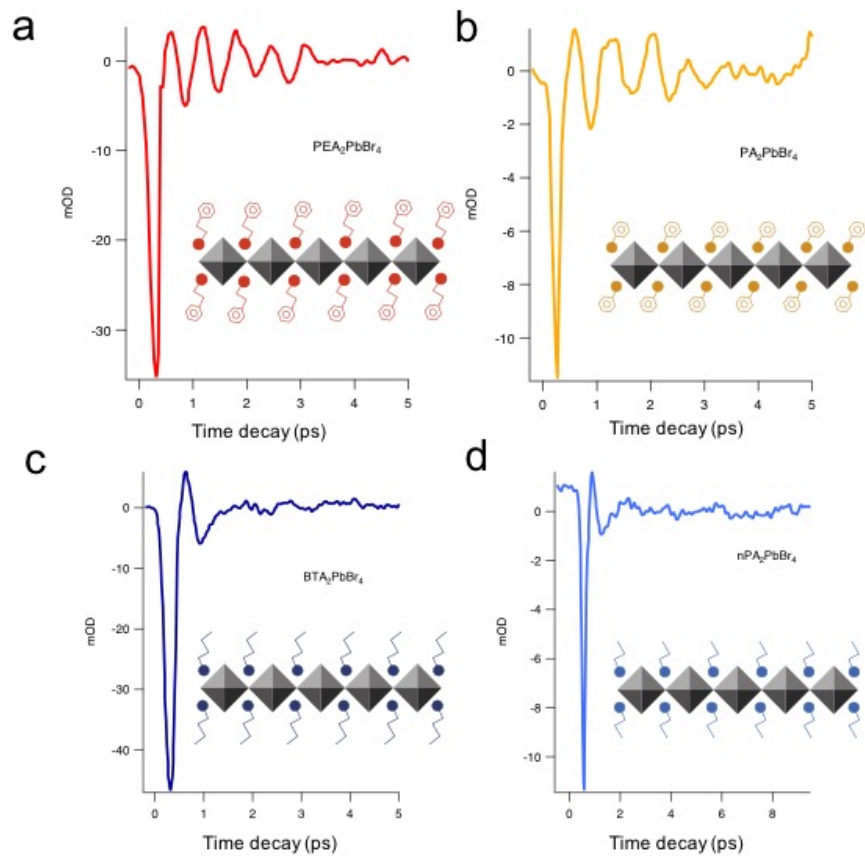


FIG. S7. Coherent phonon oscillation curves from layered perovskite ((ANH₃)₂PbBr₄) various organic cations a) Phenylethylammonium bromide, b) Phenylammonium bromide, c) Butylammonium bromide and d) n-propylammonium bromide.

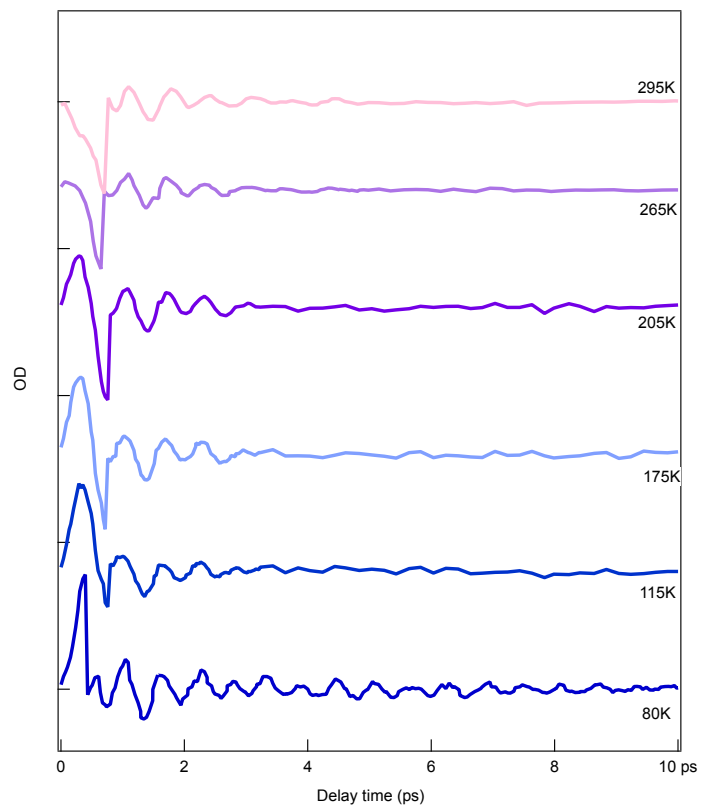


FIG. S8. Coherent phonon oscillation curves from $(\text{PEA})_2\text{PbBr}_4$ with different temperature from 80 K to room temperature.

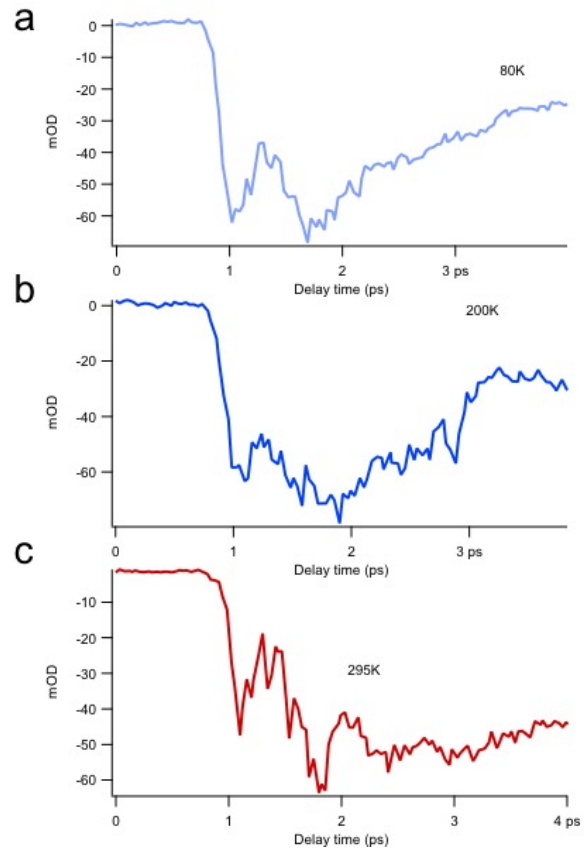


FIG. S9. Coherent phonon oscillation curves from (BTA)₂PbBr₄ at the temperature of a) 80K, b) 200K and c) 295K.

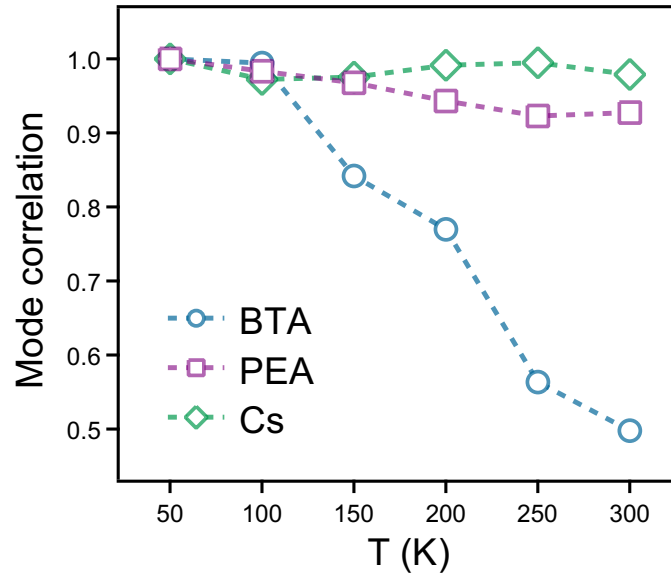


FIG. S10. Dot products between \vec{e} with the lowest frequency at 50K and \vec{e} at other temperatures, showing the correlation between modes at different temperatures. Dotted lines are used to connect neighboring symbols.

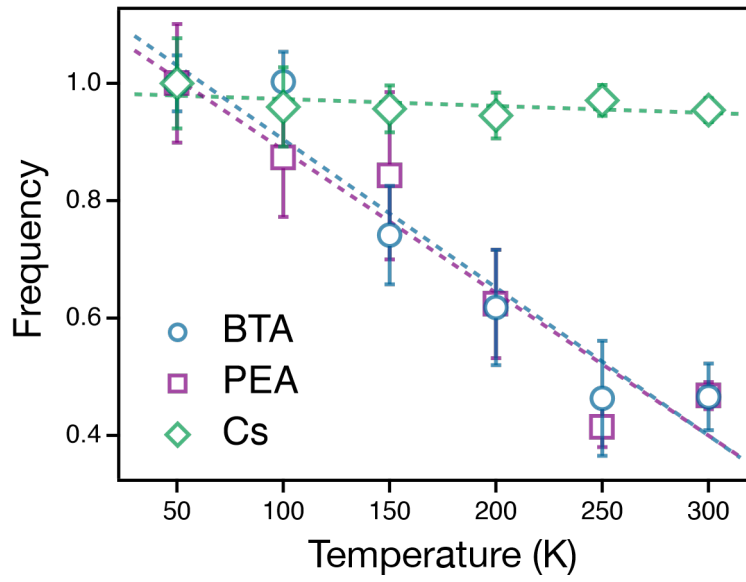


FIG. S11. Frequency of the lowest nonzero phonon mode normalized with the lowest nonzero frequency at 50K as a function of temperature. Dotted lines represent linearly fitted lines in each perovskites.

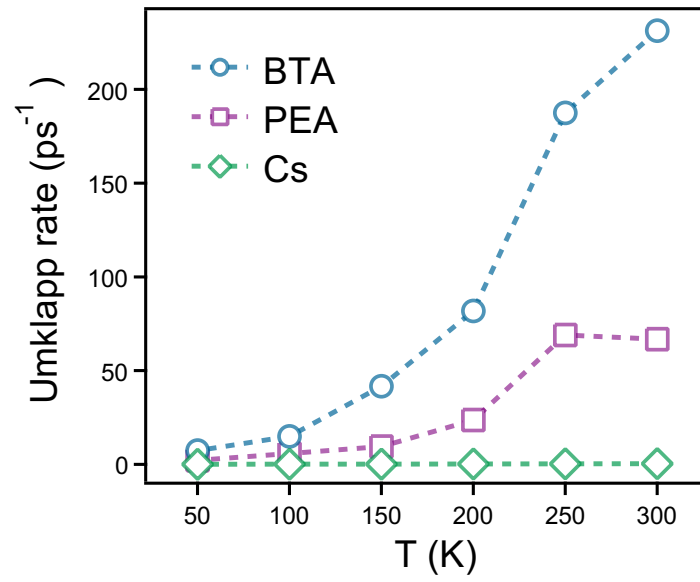


FIG. S12. Dephasing rates predicted through Umklapp scattering using Eq. S.13. Dotted lines are used to connect neighboring symbols.

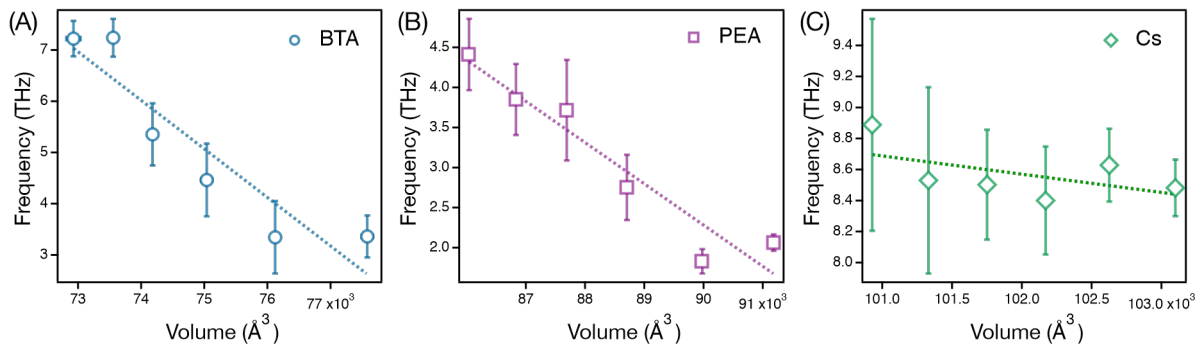


FIG. S13. Lowest optical frequency as a function of total volume of the system for (A) $(\text{BTA})_2\text{PbBr}_4$ (B) $(\text{PEA})_2\text{PbBr}_4$, and (C) CsPbBr_3 perovskites.

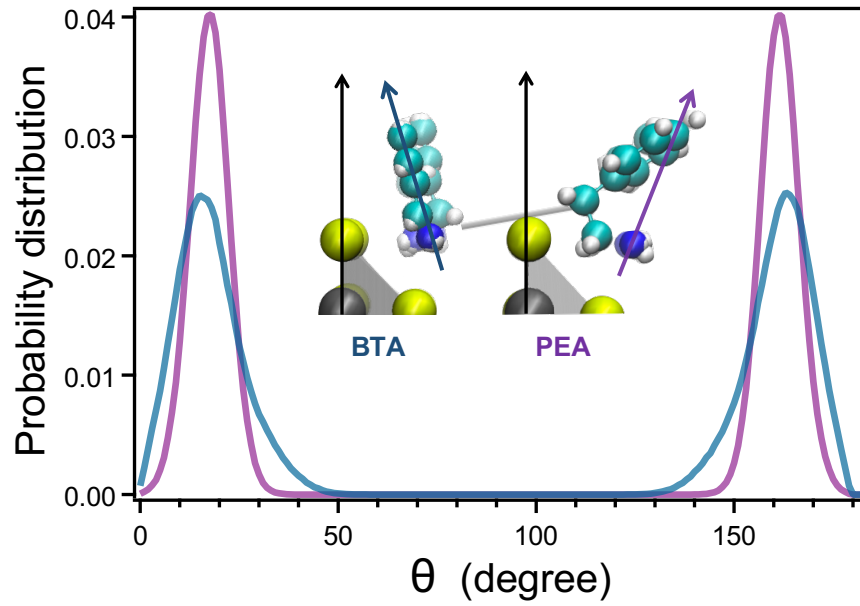


FIG. S14. Probability distribution of angles between vertical lines (black arrows) and NC vector (colored arrows) in $(\text{BTA})_2\text{PbBr}_4$ (blue line) and $(\text{PEA})_2\text{PbBr}_4$ (purple line) perovskites. Inserted figures are partial snapshots from simulations to describe NC vectors.

References

- 1 Jorgensen, W. L. & Tirado-Rives, J. Potential energy functions for atomic-level simulations of water and organic and biomolecular systems. *P Natl Acad Sci USA* **102**, 6665-6670, doi:10.1073/pnas.0408037102 (2005).
- 2 Dodda, L. S., Vilseck, J. Z., Tirado-Rives, J. & Jorgensen, W. L. 1.14* CM1A-LBCC: localized bond-charge corrected CM1A charges for condensed-phase simulations. *The Journal of Physical Chemistry B* **121**, 3864-3870 (2017).
- 3 Dodda, L. S., Cabeza de Vaca, I., Tirado-Rives, J. & Jorgensen, W. L. LigParGen web server: an automatic OPLS-AA parameter generator for organic ligands. *Nucleic acids research* **45**, W331-W336 (2017).
- 4 Martyna, G. J., Tobias, D. J. & Klein, M. L. Constant-Pressure Molecular-Dynamics Algorithms. *Journal of Chemical Physics* **101**, 4177-4189, doi:Doi 10.1063/1.467468 (1994).
- 5 Plimpton, S. Fast Parallel Algorithms for Short-Range Molecular-Dynamics. *J Comput Phys* **117**, 1-19, doi:DOI 10.1006/jcph.1995.1039 (1995).
- 6 Hata, T., Giorgi, G., Yamashita, K., Caddeo, C. & Mattoni, A. Development of a classical interatomic potential for MAPbBr₃. *The Journal of Physical Chemistry C* **121**, 3724-3733 (2017).
- 7 Wang, J. M., Wolf, R. M., Caldwell, J. W., Kollman, P. A. & Case, D. A. Development and testing of a general amber force field. *J Comput Chem* **25**, 1157-1174, doi:DOI 10.1002/jcc.20035 (2004).
- 8 Wang, J. M., Wang, W., Kollman, P. A. & Case, D. A. Automatic atom type and bond type perception in molecular mechanical calculations. *J Mol Graph Model* **25**, 247-260, doi:10.1016/j.jmgm.2005.12.005 (2006).
- 9 Lai, M. L. *et al.* Intrinsic anion diffusivity in lead halide perovskites is facilitated by a soft lattice. *P Natl Acad Sci USA* **115**, 11929-11934, doi:10.1073/pnas.1812718115 (2018).
- 10 Tu, Q. *et al.* Out-of-Plane Mechanical Properties of 2D Hybrid Organic-Inorganic Perovskites by Nanoindentation. *Acs Appl Mater Inter* **10**, 22167-22173, doi:10.1021/acsami.8b05138 (2018).
- 11 Ghaithan, H. M., Alahmed, Z. A., Qaid, S. M. H., Hezam, M. & Aldwayyan, A. S. Density Functional Study of Cubic, Tetragonal, and Orthorhombic CsPbBr₃ Perovskite. *Acs Omega* **5**, 7468-7480, doi:10.1021/acsomega.0c00197 (2020).
- 12 Welch, E. W., Jung, Y. K., Walsh, A., Scolfaro, L. & Zakhidov, A. A density functional theory study on the interface stability between CsPbBr₃ and CuI. *Aip Adv* **10** (2020).
- 13 Roknuzzaman, M., Ostrikov, K., Wang, H. X., Du, A. J. & Tesfamichael, T. Towards lead-free perovskite photovoltaics and optoelectronics by ab-initio simulations. *Sci Rep-Uk* **7** (2017).
- 14 Kong, L. T. Phonon dispersion measured directly from molecular dynamics simulations. *Comput. Phys. Commun.* **182**, 2201-2207, doi:10.1016/j.cpc.2011.04.019 (2011).
- 15 Kong, L. T., Bartels, G., Campana, C., Denniston, C. & Muser, M. H. Implementation of Green's function molecular dynamics: An extension to LAMMPS. *Comput. Phys. Commun.* **180**, 1004-1010, doi:10.1016/j.cpc.2008.12.035 (2009).

- 16 Dove, M. *Ecole thématique de la Société Française de la Neutronique* **12**, 123 (2011).
- 17 Nitzan, A. *Chemical dynamics in condensed phases (OXFORD University, 2006)* **12**, 453.
- 18 Skinner, J. L. & Park, K. Calculating vibrational energy relaxation rates from classical molecular dynamics simulations: Quantum correction factors for processes involving vibration-vibration energy transfer. *J Phys Chem B* **105**, 6716-6721, doi:DOI 10.1021/jp010602k (2001).
- 19 Moreira, R. L. & Dias, A. Comment on "Prediction of lattice constant in cubic perovskites". *J Phys Chem Solids* **68**, 1617-1622, doi:10.1016/j.jpcs.2007.03.050 (2007).
- 20 Sheldrick, G. M. A short history of SHELX. *Acta Crystallographica Section A: Foundations of Crystallography* **64**, 112-122 (2008).
- 21 Sheldrick, G. M. SHELXT—Integrated space-group and crystal-structure determination. *Acta Crystallographica Section A: Foundations and Advances* **71**, 3-8 (2015).
- 22 Sheldrick, G. M. Crystal structure refinement with SHELXL. *Acta Crystallographica Section C: Structural Chemistry* **71**, 3-8 (2015).
- 23 Dolomanov, O. V., Bourhis, L. J., Gildea, R. J., Howard, J. A. & Puschmann, H. OLEX2: a complete structure solution, refinement and analysis program. *Journal of applied crystallography* **42**, 339-341 (2009).
- 24 Momma, K. & Izumi, F. VESTA 3 for three-dimensional visualization of crystal, volumetric and morphology data. *Journal of applied crystallography* **44**, 1272-1276 (2011).